

1 **A low-cost, autonomous system for distributed snow depth 2 measurements on sea ice**

3 Ian A. Raphael,¹ Donald K. Perovich,¹ Christopher M. Polashenski,^{1,2} Robert L. Hawley³

4 ¹Thayer School of Engineering, Dartmouth College, Hanover, NH, USA

5 ²Cold Regions Research and Engineering Laboratory, US Army Corps of Engineers, Hanover, NH, USA

6 ³Department of Earth Sciences, Dartmouth College, Hanover, NH, USA

7 *Correspondence to:* Ian A. Raphael (ian.a.rafael.th@dartmouth.edu)

8 **Abstract.** Snow is a critical component of the Arctic sea ice system. With its low thermal conductivity and high
9 albedo, snow moderates energy transfer between the atmosphere and ocean during both winter and summer, thereby
10 playing a significant role in determining the magnitude, timing, and variability of sea ice growth and melt. The depth
11 of snow on Arctic sea ice is highly variable in space and time, and accurate measurements of snow depth and
12 variability are central to improving our basic understanding, model representation, and remote sensing observations
13 of the Arctic system. Our ability to collect those measurements has hitherto been limited by the high cost and large
14 size of existing autonomous snow measurement systems. We designed a new system called SnoTATOS (the Snow
15 Thickness and Temperature Observation System) to address this gap. SnoTATOS is a radio-networked, distributed
16 snow depth observation system that is 95% less expensive and 93% lighter than existing systems. In this manuscript,
17 we describe the technical specifications of the system and present results from a case study deployment of four
18 SnoTATOS networks (each with ten observing nodes) in the Lincoln Sea between April 2024 and January 2025.
19 The study demonstrates SnoTATOS' utility in collecting distributed, in situ snow depth, accumulation, and surface
20 melt data. While surface melt varied within each network by up to 38%, mean surface melt between networks varied
21 by only up to 9%. Similarly, whereas initial snow depth varied by up to 42% within each network, a comparison of
22 mean initial snow depth between networks showed a maximum difference of only 26%. This indicates that floe-
23 scale measurements made using SnoTATOS provide more representative data for regional intercomparisons than
24 existing single station systems. We conclude by recommending further research to determine the optimal number
25 and arrangement of autonomous stations needed to capture the variability of snow depth on Arctic sea ice.

26 **1 Introduction**

27 September Arctic sea ice area has diminished by ~50% since satellite observations began in 1979 (Meier et al.,
28 2023; Onarheim et al., 2018; Peng and Meier, 2018). The remainder is predominantly thin first- and second-year ice
29 (FYI, SYI) (Kwok, 2018). The Arctic Ocean may experience ice-free summers within the next decade (Jahn et al.,
30 2024). The thinning and loss of Arctic sea ice has increased Arctic coastal erosion (Barnhart et al., 2014; Eicken and
31 Mahoney, 2015), diminished habitat (Laidre et al., 2015; Post et al., 2013), impeded hunting, fishing, and
32 transportation over sea ice, and created new opportunities and uncertainties for shipping, tourism, military activity,
33 and geopolitical conflict in the Arctic (Backus, 2012; Bystrowska, 2019; Carman, 2002). Understanding the Arctic
34 ice pack is more important than ever. At the same time, rapidly changing conditions, in addition to baseline spatial

35 and temporal variability, present considerable challenges for our efforts to observe, understand, and predict changes
36 in this environment.

37 Our fundamental understanding and model representations of the Arctic sea ice system are limited by the
38 spatial and temporal resolution, consistency, coverage, representativeness, and scalability of available snow
39 observations. [Sturm et al. \(2002\) found early evidence that variability in snow cover properties, including snow](#)
40 [depth, significantly impacts heat flow, surface temperatures, ice growth, and even marine mammals.](#) Zampieri et al.
41 (2024) and Clemens-Sewall et al. (2024b) both found that neglecting sub-meter to meter-scale snow depth
42 variability results in a 10% underestimation of modeled conductive heat flux through the Arctic sea ice cover during
43 winter, yielding a directly proportional underestimation of ice growth. [Itkin and Liston \(2024\) identified meter to](#)
44 [decimeter scale snow variability as a key control on area-average heat flux, and thus ice growth. Measurements of](#)
45 [temperature profiles through the snow and ice are commonplace on observational campaigns. Augmenting these](#)
46 [temperature measurements with precise, distributed snow depth observations enables investigators to determine the](#)
47 [role of snow in controlling heat transfer at the local scale.](#)

48 Snow also influences the timing of melt onset (Holland et al., 2021), and the formation and distribution of
49 melt ponds (Polashenski et al., 2012), both of which impact the magnitude and spatial variability of sea ice melt.
50 Clemens-Sewall et al. (2024b) and Holland et al. (2021) conclude that more observations of the spatial heterogeneity
51 of snow depth are needed to improve model representations of sea ice conditions.

52 [Further, snow accumulation can impact the validity of other measurements of the Arctic system. For](#)
53 [example, an air temperature sensor initially installed at two meters effectively becomes a 1.5-meter air temperature](#)
54 [sensor after 0.5 m of snow accumulation, with a similar result occurring due to surface melt. Accurate snow](#)
55 [accumulation estimates are thus useful for interpretation of other datasets, especially those at the surface boundary](#)
56 [layer.](#)

57 Gerland et al. (2019) identified the sparsity of in situ measurements of snow depth as an essential gap in
58 our understanding of Arctic sea ice, and in a review of snow in the contemporary sea ice system, Webster et al.
59 (2018) stated that “Major questions remain … as to the exact role of snow, how it varies regionally and seasonally,
60 how snow conditions on sea ice are changing and what effects these changes have on the atmosphere–sea ice–ocean
61 interactions,” and that, “first and foremost, our limited understanding stems from the complexity of the snow–sea ice
62 systems and the scarcity of observations.” In short, we need high-spatial-resolution observations of snow depth to
63 constrain spatial variability, validate remote sensing observations, advance model physics, and maintain an
64 observational record of snow depth in the Arctic.

65 Remote sensing observations give broad and consistent geographical coverage, but do not afford the
66 necessary spatial resolution or measurement precision (Meier and Markus, 2015; Webster et al., 2018). Crewed, in
67 situ drift and station experiments – e.g., the 1997–1998 SHEBA expedition (Perovich et al., 1999, 2003; Sturm et
68 al., 2002), the 2015 N-ICE experiment (Granskog et al., 2018; Merkouriadi et al., 2017; Rösel et al., 2018), the
69 2019–2020 MOSAiC expedition (Itkin et al., 2023; Nicolaus et al., 2022; Raphael et al., 2024), and the long-running
70 Russian drifting ice station program (Colony et al., 1998; [National Snow and Ice Data Center, 2004](#)) – are
71 important, but only partial, solutions. They provide opportunities to densely sample sea ice and snow conditions,

Deleted:

Deleted:

Deleted: -2016

Deleted: 2018-

Deleted: 2

77 usually alongside a rich suite of atmosphere, ocean, and contextual information. However, each expedition offers
78 only a snapshot in space and time.

79 Autonomous in situ instruments can provide wide spatial coverage and high temporal resolution, and
80 several autonomous systems exist that offer precise, in situ measurements with selectable sampling frequency and
81 up to 1–2 year endurance (Liao et al., 2019; Nicolaus et al., 2021; Planck et al., 2019). These systems are regularly
82 deployed in the Arctic, but are expensive, heavy, and difficult to transport to and in the field (Table 1). This has
83 historically limited their use to one to two instruments installed per floe, and few (<10) per region, the rare
84 exceptions being major expeditions like N-ICE (Itkin et al., 2017; Nicolaus et al., 2021) and MOSAiC (Nicolaus et
85 al., 2022; Rabe et al., 2024). Even on such major campaigns, relatively few units have been deployed on a single
86 floe. These limited point measurements are usually taken as representative local snow depths. However, snow depth
87 on Arctic sea ice can vary by ~~two~~ orders of magnitude over decimeter to kilometer length-scales due to
88 topographical features, surface conditions of the underlying ice and snow, and ice age (and resultant accumulation
89 time), among other factors (Clemens-Sewall et al., 2024a; Iacozza and Barber, 1999). A point measurement is
90 unlikely to capture the mean (and, by definition, cannot capture the variance) of snow depth in complex local snow
91 fields.

92 We need a new snow sensing technology that will improve the spatial density of Arctic snow depth
93 measurements. The system must be inexpensive, easy to transport, use, and install, and have similar measurement
94 precision and endurance to existing systems. We have designed, built, tested, and deployed the Snow Thickness and
95 Temperature Observation System (SnoTATOS) to meet this need (Table 1). SnoTATOS is an autonomous, radio-
96 networked, distributed snow depth measurement system that will accurately observe the mean and variance of snow
97 depth on Arctic sea ice at meter to regional spatial scales. Throughout the design process, we focused on
98 affordability; ease of manufacturing, transport, use, and deployment; and matching or exceeding existing
99 measurement standards. Our ultimate goal is to reduce or eliminate barriers to deploying the system in large
100 numbers across the Arctic. [The SnoTATOS system is also a valuable tool for distributed observations of terrestrial](#)
101 [snow, such as in alpine, tundra, and glacier environments.](#)

102 In this manuscript, we describe the characteristics of the SnoTATOS system, share bench-testing
103 performance evaluations, and present results from SnoTATOS prototype networks deployed in the Lincoln Sea in
104 May 2024.

105 **Table 1:** Specifications of several polar snow depth measurement systems (all specifications are per unit/station)

System	Approximate cost	Weight	Size	Time to deploy	Endurance	Measurement precision ^a
MetOcean Snow Buoy	\$9,400 USD	40 kg	2.55 m x 1 m x 1 m	30–40 min	12–18 months	± 1 mm
SAMS SIMBA buoy	\$10,000 USD	25 kg	~0.55 m x 0.30 m x 0.20 m	20–30 min	> 12 months	± 2 cm

Deleted: 2

Deleted:

Formatted Table

SIMB3	\$18,000 USD	36 kg	4.87 m x 0.25 m x 0.11 m	20–30 min	24 months	± 1 mm
SnoTATOS	\$500 USD ^b	1.8 kg	2.44 m x 0.15 m x 0.1 m	<10 min	4.5 years ^c	± 1 mm

^aThis value specifies the instrument's stated measurement precision, not the accuracy of the snow depth retrieval.

The precision of the ultrasonic rangefinders is ± 1 mm, while accuracy depends on temperature compensation, ice/snow surface conditions, sensor icing, etc. The precision of digital temperature chain instruments (e.g., the SIMBA) is ± 2 cm (the separation between any two temperature sensors in the chain), while the accuracy depends on the thermal characteristics of the snow, ice, and atmosphere, which affect the feasibility of determining the interfaces between the three media.

^bCost of components only (not including manufacturing and assembly) is approximately \$200.

^cThis is a nominal endurance based on power consumption measurements in a laboratory setting. We expect the effective endurance to be reduced by low temperatures and any radio communication reattempts.

2 System description

2.1 Overview of SnoTATOS

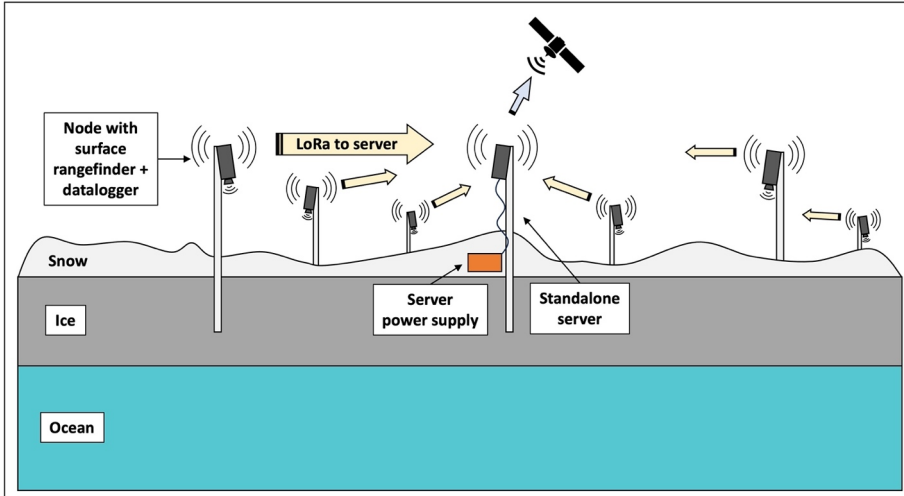
A standard SnoTATOS network consists of several autonomous snow measurement stations (hereafter called “nodes”) linked to a central server by a LoRa radio network (Augustin et al., 2016) (Fig. 1). The number of nodes in a network is theoretically unlimited. Each node is equipped with an ultrasonic rangefinder (HRXL-MaxSonar-WR Datasheet, 2024) for monitoring the snow or ice surface position; additional sensors (e.g. temperature sensors) can be added with minimal engineering effort. The network is synchronized such that all nodes simultaneously collect samples and transmit their data back to the server at regular intervals, with random transmission jitter introduced to reduce packet collisions. The sampling frequency is programmable with a typical interval set at four hours. We initially designed the server to integrate into a SIMB3 ice mass balance buoy (Planck et al., 2019, p.201), thereby taking advantage of the SIMB3’s existing Iridium telemetry. We have since redesigned the server to operate in a freestanding mode, either transmitting data using its own Iridium telemetry module or storing data locally on an SD card. In the following sections, we will describe the node and server electronics, physical characteristics, radio network, and operating software.

Deleted: The

Deleted: can also

Deleted: to a landside server

Deleted: satellite



137
138
139
140
141

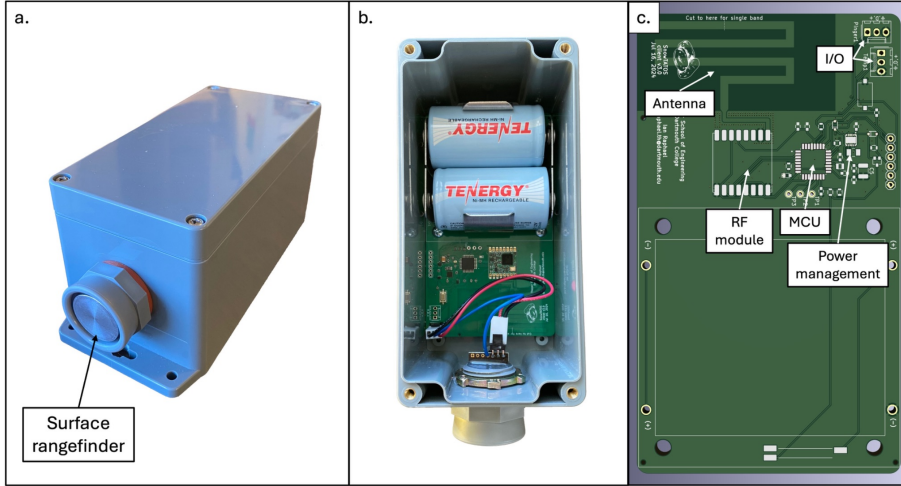
Figure 1: Diagram of a SnoTATOS network. SnoTATOS data is collected at each node in a distributed network, and transferred to the server via radio, either directly (in the hub-and-spoke network model) or via relay through peers (in the mesh network model). The server collects all SnoTATOS data and relays it to the SIMB3, which handles satellite telemetry to a land-side server.

142

2.2 Node overview and physical characteristics

143
144
145
146
147
148
149
150
151
152
153
154

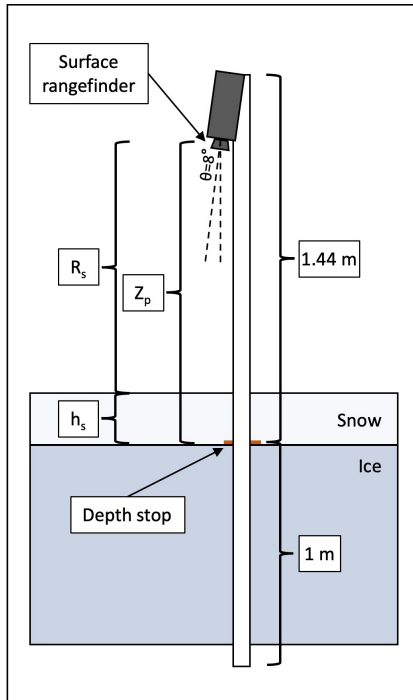
A SnoTATOS node consists of a MaxBotix 7389-200 ultrasonic surface rangefinder; a microcontroller that manages sampling, datalogging, and radio communications with the server; a nickel-metal hydride (NiMH) battery power-bank; and ancillary electronics. Figure A1 shows a system block diagram. The electronics are housed in a watertight plastic enclosure (Fig. 2). The rangefinder is mounted directly to a sidewall of the enclosure (Fig. 2). The resulting sensing unit is 0.08 m x 0.19 m x 0.09 cm and weighs approximately 0.62 kg. The sensing unit is mounted on a 2.44 m x 0.038 m x 0.038 m (8 feet x 1.5 inches x 1.5 inches) wooden stake (Fig. 3). The long edges of the stake are filleted so that the stake fits snugly in a standard 5 cm (2 inch) diameter ice auger hole. The total weight of an individual node is approximately 1.80 kg, representing a 96% mass reduction compared to the MetOcean Snow Buoy. The stake length maximizes the range of observable snow depths while [ensuring ease of transport to field sites by conforming to less-than-truckload \(LTL\) and passenger aircraft lower deck freight limitations, where freight often must be less than approximately 2.44 m long](#).



155
156 **Figure 2: SnoTATOS node sensing unit.** Panel (a) is a photograph of a SnoTATOS sensing unit, showing
157 the ABS plastic enclosure and ultrasonic surface rangefinder mounted in the sidewall of the enclosure.
158 Panel (b) is a top down photograph of the sensing unit with lid removed, showing the PCB, rangefinder
159 wiring harness, and battery bank. Panel (c) shows an annotated digital model of a node PCB with key
160 features identified.
161

162 The Maxbotix ultrasonic rangefinder detection cone has an approximately 40° aperture angle, so spurious
163 detection of the mounting stake was a significant design concern. We conducted a series of experiments to
164 determine the optimal sensor look-angle (θ) and standoff of the sensor from the mounting stake. We determined that
165 a sensor standoff between 5–40 cm and $5^\circ < \theta \leq 35^\circ$ yielded the lowest error rate (between 4–6%). Taking this into
166 account, we mounted the enclosure on an inclined face of the stake, with $\theta = 8^\circ$ off-nadir and a standoff of 0.05 m.
167 The rangefinder's projected beam has a roughly circular footprint with a diameter of approximately 0.60 m at typical
168 ranging distances.

169 During installation, a 5 cm (2 inch) diameter hole is drilled into the ice and the stake is inserted until a
170 depth stop is at the ice surface, then allowed to freeze in. The initial snow depth and distance between the snow
171 surface and rangefinder are then measured. The rangefinder is thus situated at a known height (Z_p) above the ice
172 surface, and subsequent snow depth (h_s) can be determined from the range value (R_s) as $h_s = Z_p - R_s$. Through
173 experimental measurements we have determined that the range reading does not vary appreciably for $5^\circ < \theta \leq 35^\circ$,
174 so we do not perform a trigonometric correction for R_s . The installation process requires ~2 to 10 minutes per node
175 depending on conditions, reducing deployment time by at least 50% compared to other systems.
176



177
178 **Figure 3: Schematic diagram of a SnoTATOS node.** Snow depth (h_s) can be calculated by subtracting the
179 range reading (R_s) from the rangefinder offset (Z_p). ▼

Deleted: Through experimental measurements we have determined that the range reading does not vary appreciably for $5^\circ < \theta \leq 35^\circ$, so we do not perform a trigonometric correction for R_s .

180 **2.3 Sensing unit electronics**

181 Here, we summarize the selection of key components in the sensing unit and their notable features. The sensing unit
182 is built around an ATmega4808 AVR microcontroller unit (MCU). The ATmega4808 is an 8-bit reduced instruction
183 set computer (RISC) (Patterson, 1985) with 48 KB of program memory and 6 KB of RAM. The chip is equipped
184 with an onboard 10-bit analog-to-digital converter (ADC). We added an external crystal oscillator which drives a
185 one-second precision system clock, enabling an ultra-low-power standby mode with programmable, alarmed
186 wakeups. In standby mode, unused peripheral devices are depowered and the MCU sleeps until woken, either by a
187 programmed alarm or by an external interrupt on a general-purpose input/output (GPIO) pin. We selected the
188 ATmega4808 for its low power consumption, affordability, and programming simplicity. The MCU has an operating
189 input voltage range of 1.8–5.5 V, however, logic levels and GPIO output voltage are dependent on MCU input
190 voltage. We added a low-quiescent-current (0.3 μ A) buck-boost converter with a 1.8–5.5 V input voltage range and
191 a fixed 3.3 V output. This achieves 3.3 V board logic and GPIO output voltage while maintaining flexibility in
192 power supply voltage (Table 2).

197 We selected the HopeRF RFM95-915 LoRa module for radio communications. The module operates at 915
198 MHz with a maximum output power of 20 dBm. The 902–928 MHz frequency range is a license-free Industrial,
199 Scientific, and Medical (ISM) radio band in the Americas (including the United States, Greenland, Canada, and
200 South and Central America). The unit is directly exchangeable for the RFM95-868, which operates at 868 MHz,
201 within the European ISM band (including [the Russian Federation](#)). These two options ensure system compliance for
202 any Arctic deployment. Either option is suitable for deployments in international waters. The authors are not aware
203 of any regulations restricting radio frequency use in Antarctica.

204 Most snow accumulation observation systems use one of several models of the Maxbotix ultrasonic
205 rangefinder. Maxbotix offers many variations of their basic rangefinder, including snow-specific models. We chose
206 to use their general-purpose model with the compact horn option (MB7389-200).

207 We use NiMH batteries for the power bank due to their improved cold-weather performance vs. alkaline
208 batteries (Fetcenko et al., 2007) and less stringent shipping regulations compared to lithium-ion batteries. We used
209 Tenergy Power D-cells, rated to 10,000 mAh per cell. Each node has a power bank of 4-cells, arranged in two
210 parallel pairs of two cells in series. A NiMH battery has a functional voltage of ~1.2 V for most of its discharge life
211 in normal conditions, yielding a nominal supply voltage $V_n = 2.4$ V and a nominal energy capacity of 24 Wh.

212 We designed a custom printed circuit board (PCB) to integrate all components (Fig. 2). The PCB is a two-
213 layer board designed on a 1.6 mm FR-4 substrate. We designed a monopole PCB trace radio antenna adapted from a
214 Texas Instruments design (Wallace, 2013).

216 **Table 2: SnoTATOS electrical characteristics**

	<u>Nominal input voltage</u>	<u>Input voltage operating range</u>	<u>Average power demand</u>
<u>Node</u>	<u>2.4 V</u>	<u>1.8-5.5 V</u>	<u>610 μW</u>
<u>Server (standalone)</u>	<u>9.0 V</u>	<u>5.1-36.0 V</u>	<u>15.54 mW</u>
<u>Server (SIMB3 integrated)</u>	<u>18 V</u>	<u>3.4-36.0 V</u>	<u>18.54 mW</u>

217

218 2.4 Server electronics

219 The SnoTATOS server uses the same MCU, radio module, and antenna design as the node sensing units. However,
220 the server is not equipped with sensors. [In freestanding mode, the server is equipped with a RockBLOCK 9603](#)
221 [Iridium Short Burst Data \(SBD\) modem. The standalone server is equipped with a 9 V, 388 Wh NiMH power](#)
222 [supply. A Pololu D24V5F5 buck converter steps the supply voltage down to 5 V to supply the RockBLOCK 9603](#)
223 [unit, and a Pololu D24V5F3 buck converter steps the supply voltage down to 3.3 V to supply the server MCU.](#)

224 [When integrated into the SIMB3 buoy, the server is designed to use the SIMB3's 18 V power supply. We](#)
225 [used a Pololu D24V5F5 buck converter to step the 18 V SIMB3 supply down to 5 V \[to supply the server MCU.\]\(#\) We](#)
226 [integrated all components using a custom PCB similar to the node PCB.](#)

Formatted: Complex Script Font: Bold

Formatted Table

Formatted: Indent: First line: 0"

Deleted: Further

Deleted: ,

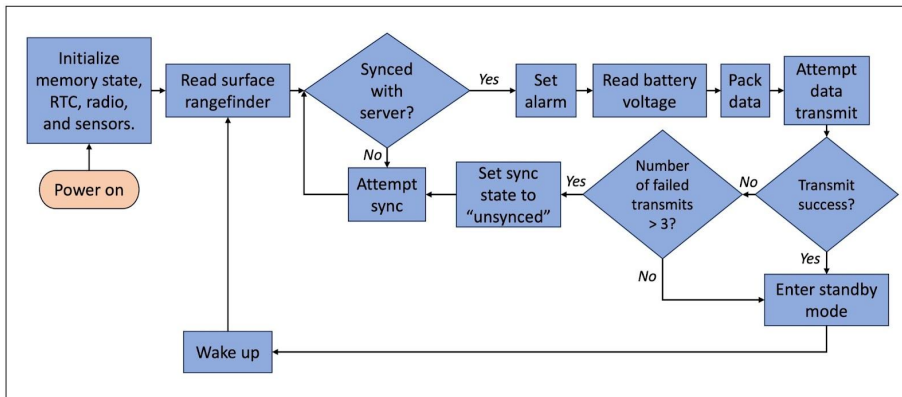
Formatted: Indent: First line: 0.5"

229 **2.5 Software**

230 **2.5.1 Node operations**

231 The system software is written in C and C++, using the Arduino hardware abstraction layer (HAL) to interface with
232 the MCU. The nodes follow the high-level logical flow shown in Fig. 4. When powered on, the node enters the
233 `Setup` function, where it initializes the memory state, system clock, radio module, and rangefinder, and sets
234 input/output pin states. The node then moves into the `Loop` function, where it will remain for its lifetime unless it is
235 power-cycled. In `Loop`, the node first samples the rangefinder to obtain a snow depth reading at “wake-up” time.
236 The node then checks its synchronization state. If it is not synced with the server (as is the case upon initial power-
237 up), it will wait at this stage until it receives a synchronization broadcast message from the server. After
238 synchronizing with the server, the node immediately sets an RTC alarm to wake after the appropriate elapsed time
239 (the sampling interval). The node then reads its battery voltage, packs this and the rangefinder data into a buffer, and
240 attempts to transmit the buffer to the server. If the transmission is successful and acknowledged by the server, the
241 node depowers all unnecessary peripherals and enters a deep sleep state until triggered by the RTC alarm. However,
242 if more than three *unsuccessful/unacknowledged* transmissions occur, the node returns to an unsynced state and
243 remains awake until resyncing with the server. We implemented this failsafe to prevent network failure in case of
244 clock drift or other errors resulting in network desynchronization over the course of the deployment.

245



246
247
248
249

Figure 4: Node flow diagram. The high-level logic of a SnoTATOS node equipped with only a snow surface rangefinder is shown. Additional sensors may be added, which would be read at the same stage as the surface rangefinder.

250 **2.5.2 Radio communications**

251 The radio network is implemented using LoRa, a long-range, low-power radio technology (Augustin et al., 2016).
252 Nominal LoRa radio ranges are up to 10–20 km with clear line of sight. The RFM95 LoRa transceiver manages the
253 physical layer of the Open Systems Interconnection (OSI) network model (Zimmermann, 1980), handling bitwise

254 data encoding, chirp spread spectrum (CSS) modulation, and physical transmission of the data. We used the open
255 source [RadioLib](#) library (RadioLib - Arduino Reference, 2024) to implement the data link layer atop the physical
256 layer; this handles data-packet to dataframe formatting and the digital interface between the MCU and the RFM95
257 module.

258 We developed software to implement the Network, Transport, Session, and Presentation layers of the OSI
259 model. These handle data packet assembly, addressed packet transmission, packet receipt acknowledgment, failed
260 transmission reattempts, packet transmission timeouts, and network collision handling. These are well established
261 general concepts in computer networking, which we implemented in a lightweight C++ library for handling small-
262 packet data transmission in an addressed, reliable network, with options for either hub-and-spoke or mesh network
263 topologies. We gave particular attention to robust packet acknowledgement and secure server–node transactions,
264 since this reduces network airtime for each node (by preventing unnecessary reattempts), in turn reducing potential
265 node–node collisions. This results in a more reliable network, with less power expended on multiple transmission
266 reattempts and unnecessary node waketime.

267 The system’s standard network topology is the hub-and-spoke model, where individual nodes (the
268 “spokes”) communicate directly with the server (the “hub”). This network topology is simple to implement and is
269 also typically the least power-intensive network model. In this topology, network sizes are limited by the 10–20 km
270 nominal LoRa range. [This range assumes](#) line-of-sight between node and server. [However, range and reliability may](#)
271 [be reduced](#) in complex terrain, such as in highly deformed sea ice where direct line-of-sight between the server and
272 each node may not be possible [since the sensing unit sits approximately 1.44 m above the ice surface \(Figure 3\),](#)
273 [while ridges can reach a height of several meters \(Duncan et al., 2018\).](#) We implemented an alternative mesh
274 network topology to address this limitation, [where data from out-of-range nodes can be relayed to the server through](#)
275 [peers.](#) We use a naive flooding protocol (Zahn et al., 2009) with acknowledged packet receipt. A detailed description
276 of the node-side mesh network implementation is included in Appendix B.

277 2.5.3 Server operations

278 The server follows the high-level logical flow shown in Fig. 5. When powered on, the server enters the `Setup`
279 function, where it initializes its memory state, system clock, radio module, SIMB3 communications (if integrated
280 into SIMB3), and sets input/output pin states. The server then moves into the `Loop` function, where it will remain
281 for its lifetime unless it is power-cycled. In `Loop`, the server first sets a “bedtime” alarm, which will trigger when
282 the server wake-period ends and it is time for the server to enter standby mode. It then broadcasts a sync message to
283 the network, and proceeds to loop through two stages until the bedtime alarm triggers.

284 In the first stage, the server checks to see if it has received a message from a node. If it has, it writes the
285 node’s data to the appropriate location in its memory buffer for later [Iridium telemetry \(standalone server\)](#) or
286 transfer to SIMB3 ([integrated server](#)), then returns an ACK message to the originating node. In the standard hub-
287 and-spoke topology, this is a unicast message directly to the originating node. A description of the server-side mesh
288 network operations is included in the Appendix B.

Deleted: given

Deleted: R

Deleted: impeded

Deleted: e.

Deleted: .

294 If the server is operating in standlone mode, it continues to listen for data from nodes until it is time to
295 sleep. When it is time to sleep, the server sets a wakeup alarm corresponding to the sampling interval, transmits its
296 data via Iridium, and enters standby mode. If the server is integrated into a SIMB3, the server adds a second stage
297 during its waketime loop. In the second stage, the server checks to see if the SIMB3 has requested the data from the
298 server. If the SIMB3 has requested data, the server passes the buffer to the SIMB3, then resets the buffer to default
299 values. The server continues checking these two conditions (“Received data from a node?” and “SIMB3 requested
300 data?”) until it is time to sleep, at which point it will set a wakeup alarm and enter standby mode. Despite the server
301 checking the “SIMB3 requested data?” condition multiple times, the SIMB3 is expected to request data only once
302 during a given sampling interval. However, due to communications protocols between the SIMB3 and the server, it
303 is beneficial to respond to any hypothetical SIMB3 request as legitimate, even if the server responds with default
304 buffer values.

305 Under normal conditions, all nodes are expected to have transmitted their data to the server before the
306 server transmits data, either via Iridium or to the SIMB3. The server will not wait for all nodes to transmit before
307 transmitting data; this prevents the server from becoming unresponsive if a node fails to transmit or is otherwise
308 inoperable. ▲

Moved (insertion) [1]

Deleted: an

Deleted: alarm corresponding to the sampling interval

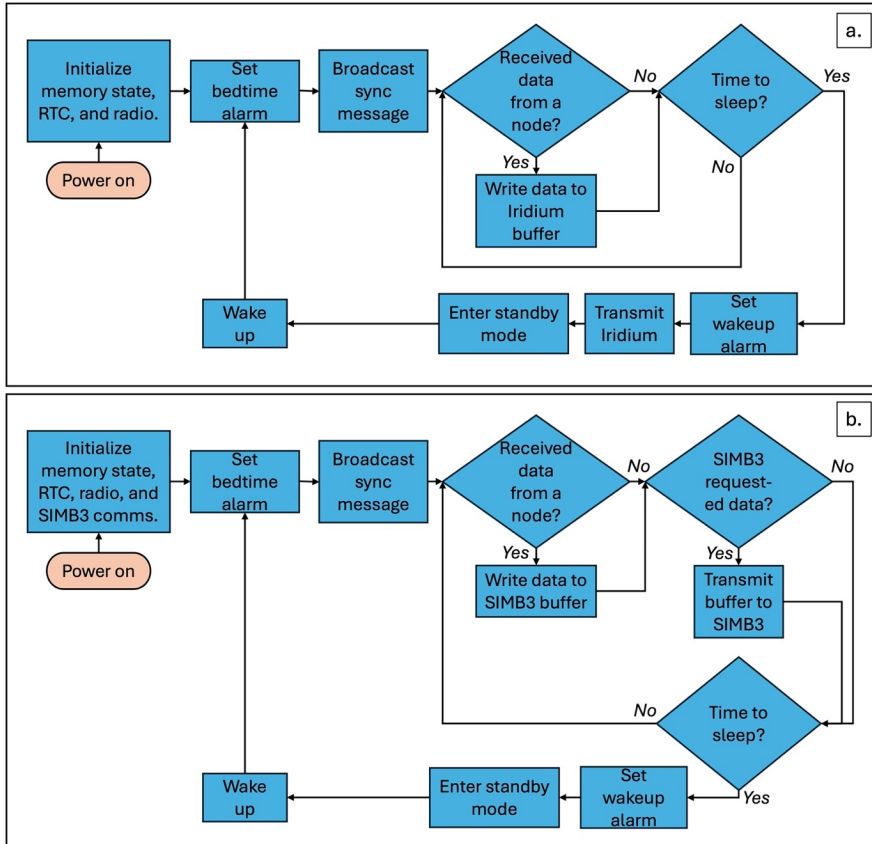
Deleted: ¶

Deleted: SIMB3 requests data

Deleted: passing data to the SIMB3

Deleted: hanging

Moved up [1]: The server continues checking these two conditions (“Received data from a node?” and “SIMB3 requested data?”) until it is time to sleep, at which point it will set an alarm corresponding to the sampling interval and enter standby mode. Despite the server checking the “SIMB3 requested data?” condition multiple times, the SIMB3 is expected to request data only once during a given sampling interval. However, due to communications protocols between the SIMB3 and the server, it is beneficial to respond to any hypothetical SIMB3 request as legitimate, even if the server responds with default buffer values.



326
 327 **Figure 5: Server flow diagram.** Panel (a.) shows the high-level logic flow for a standalone SnoTATOS
 328 server, and panel (b.) shows the high-level logic for a server integrated into a SIMB3 buoy.

329 **2.6 SIMB3 integration**

330 We used the I2C (Inter-Integrated Circuit) protocol to establish communications and data transfer between the server
 331 and the SIMB3. I2C is a serial communication protocol that allows a controller device (in this case, the SIMB3) to
 332 query packetized data from an addressed target device (the server). In addition to the standard I2C SDA (serial data)
 333 and SCL (serial clock) lines, we added a low-active chip select line (CS). The server and SIMB3 share a common
 334 ground line. When the SIMB3 is preparing to retrieve data from the server, it sets the CS line to ground (0 V) to
 335 notify the server. The server then prepares the data buffer for the SIMB3 and stands by until the SIMB3 retrieves the
 336 data through an I2C request or the transaction has timed out. The SIMB3 adds the retrieved data to its existing
 337 Iridium message and transmits it to a land-side server.

Deleted: T

Deleted: of

Deleted:

Deleted: that is

Deleted: is shown

Deleted: The server may also operate in standalone mode. In this case, the SIMB3 communications stages would be eliminated, and an Iridium telemetry stage would be added....

Deleted: pulls

348 **2.7 Bench tested power characteristics**

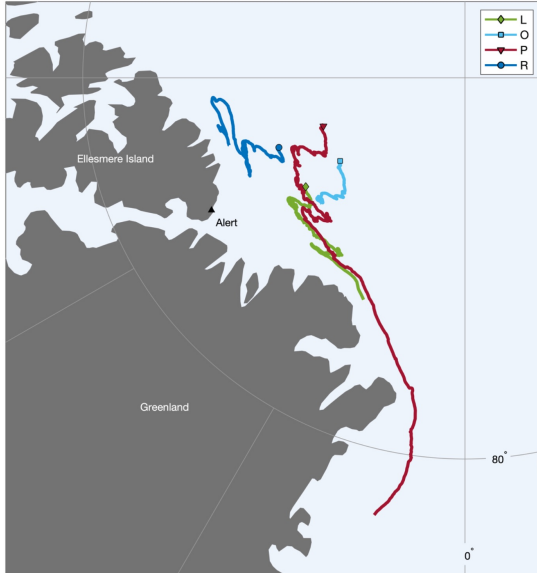
349 We performed laboratory tests to estimate the power characteristics of the sensing unit using the shunt-resistor
350 method and linear circuit analysis. By measuring the voltage drop, V_r , across a resistor with a known and low value,
351 R , one can use Ohm's law ($V_r = IR$) to determine the corresponding circuit current, I . With a known supply voltage,
352 V_s , one can then use the power law ($P = IV$) to determine the circuit power demand, P . We used an oscilloscope to
353 make time-resolved voltage measurements through all phases of the node's operating cycle, then converted these
354 measurements to time-resolved power (Fig. A2).

355 We tested over a range of supply voltages that the node might typically experience, from $V_s = 1.6$ V (below
356 the buck/boost converter threshold of 1.8 V) to $V_s = 3.3$ V (above the nominal battery bank supply voltage,
357 $V_n = 2.4$ V). We determined that at $V_s = V_n = 2.4$ V, the average circuit current across all phases of the typical 4-
358 hour duty cycle is 254 μ A, and the average power demand is 610 μ W. With a 24 Wh power bank (two 10,000 mAh
359 D-cell batteries), each node has an estimated endurance of \sim 1,639 days, or \sim 4.5 years (far longer than the lifetime of
360 any sea ice on which it is likely to be installed). However, this does not account for battery efficiency losses due to
361 cold temperatures, nor atypical conditions such as radio transmission retries.

362 We conducted similar power tests for the server, finding an average current draw of 1.03 mA at $V_s = 18$ V,
363 yielding an average power demand of 18.54 mW. This is approximately 30% of the SIMB3's power budget (Planck,
364 2021), yielding an estimated endurance of approximately 560 days, or slightly more than 1.5 years. Operating in
365 standalone mode, the power supply can be reduced to $V_s = 3.4$ V, increasing efficiency and reducing average power
366 demand to approximately 2,500 μ W. This produces a nominal endurance of 4.4 years with a 96 Wh battery bank
367 (eight 10,000 mAh D-cell batteries).

368 **3 Case study, Lincoln Sea, April 2024–January 2025**

369 We deployed four SnoTATOS networks in the Lincoln Sea in late April and early May, 2024, during the NASA
370 ARCSIX project (McNamee, 2024) (Fig. 6). Each network consisted of ten nodes and a server integrated into a
371 SIMB3 buoy. We deployed the networks in multiyear ice just before the onset of surface melt. We placed the nodes
372 randomly between 25 and 200 m from each buoy, with clear line-of-sight to the buoy. We measured initial snow
373 depth at each node, and ice thickness and snow depth at each SIMB3. As of 3 January, 2025, three networks (2024L,
374 2024O, and 2024R) were no longer reporting. The failure of 2024O is consistent with an I2C communications
375 failure between the server and SIMB3 MCU. The steady attrition of nodes and their location in a shear band suggest
376 that networks 2024L and 2024R were destroyed by ice dynamics. 2024P continues to report, with four nodes
377 surviving; the rest were likely destroyed by ice dynamics. We will now describe the general results from these
378 installations. We include data from network 2024O in summary visualizations for completeness, however, we do not
379 consider these data in our analysis.



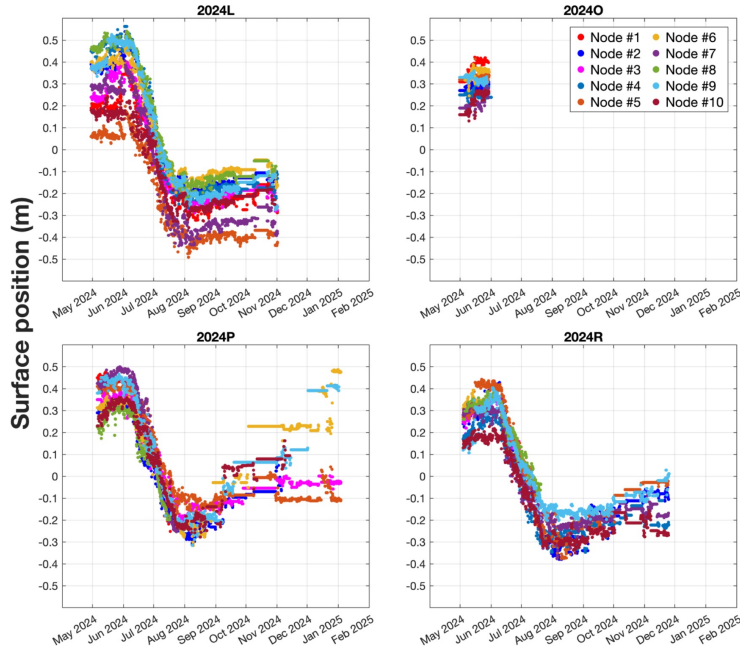
380
381 **Figure 6: Drift tracks of four SnoTATOS networks deployed in the Lincoln Sea in April and May,**
382 **2024.**

383 The mean [conditions for all nodes at the time of installation of each of](#) the four networks are given in Table

384 [Deleted: installation conditions for](#)

385 [Deleted: 2](#)

386 [3](#) The time series of snow depth and surface melt for all nodes at each network is shown in Fig. 7. We observed
387 between 0.05 and 0.10 m of snow accumulation at each network between installation in late April and late May.
388 Surface melt in the region began in late May, after which snow depth decreased steadily at all nodes, reaching 0 m
389 between 12 June and 8 July. On average, snow persisted longest at network P, which also had the deepest initial
snow cover (Fig. 8). Ice surface melt then commenced, continuing until early August (Fig. 9).



392
 393 **Figure 7: Time series scatterplots of surface position at four SnoTATOS networks.** Time series data of
 394 surface position is shown for each node at the four ARCSIX SnoTATOS networks. “Surface position” is the
 395 position of the surface sensed by the ultrasonic rangefinder (air–snow or air–ice interface) relative to the
 396 initial snow–ice interface (surface position 0). Each node initially demonstrates a positive surface position
 397 value, indicating a positive snow depth. Snow depth increases until around early June at all nodes. Snow melt
 398 then begins around mid-June, continuing at each node until the surface position reaches 0, indicating
 399 complete snow melt and the onset of ice surface melt. Ice surface melt continues until early August. From
 400 that point on, any positive change in surface position indicates new snow accumulation.

401
 402 The results show substantial variability in initial snow depth, magnitude and timing of surface melt, and
 403 snow accumulation. Mean initial snow depths varied between networks by up to 26% (0.23 m at R vs. 0.31 m at L
 404 and P). Within the networks, initial snow depth variability ranged from 26% at network R to 42% at network L.

405
 406 **Table 3: ARCSIX summary conditions**

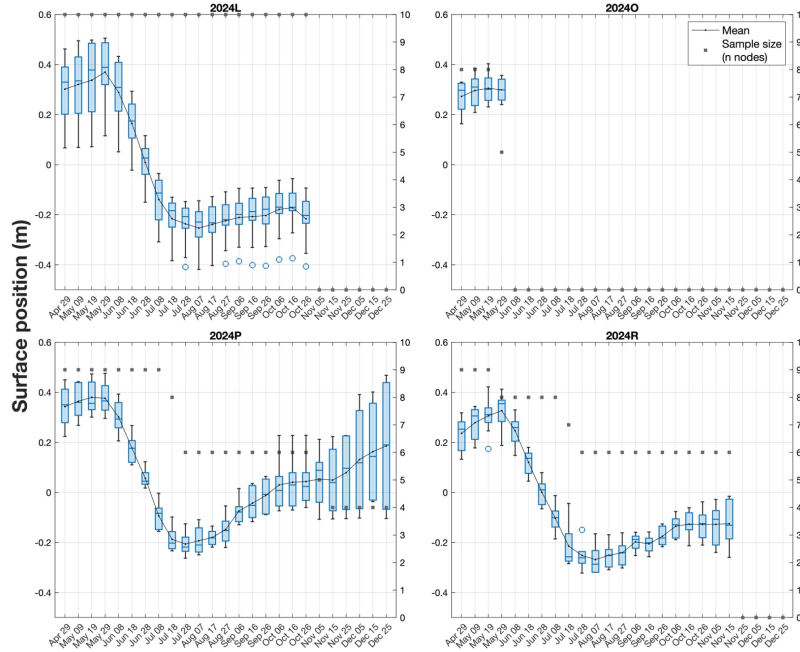
Network name	Duration	Initial ice thickness (m)	Mean initial snow depth \pm standard deviation (m)	Mean ice surface melt (m)	Mean combined ice equivalent surface melt (m)	Site description

Deleted: 2

Formatted Table

2024L	29 April–1 November, 2024	1.96	0.31 ± 0.13	0.23 ± 0.11	0.33 ± 0.08	Level multiyear ice (MYI) floe. Potential hummocks which snow has filled, rendering a smooth surface.
2024O	5 May–1 June, 2024	1.72	0.29 ± 0.09	~	~	Large MYI or SYI pan with relatively level surface. May have experienced little surface melt.
2024P	6 May, 2024–3 January, 2025 ^a	2.16	0.31 ± 0.10	0.20 ± 0.06	0.31 ± 0.05	Hummocky MYI floe in ridged area. Floe too thick to drill in some places (> 4 m).
2024R	4 May–25 November, 2024	2.40	0.23 ± 0.06	0.23 ± 0.11	0.30 ± 0.11	Hummocky MYI floe.

408 ^aFour nodes from network P were still reporting as of 3 January, 2025.



409
 410 **Figure 8: Box-and-whisker time series of surface position at four SnoTATOS networks.** Each box-and-
 411 whisker shows the spatial distribution of the ten-day-average surface position for a given network. The lower
 412 and upper edge of each box show the first and third quartiles, the bar in the box shows the median, and the
 413 whiskers indicate the minimum and maximum non-outlier values. Outliers are shown as open blue circles,
 414 and are defined as more than 1.5 times the interquartile range lesser or greater than the first and third quartiles,
 415 respectively. The small, dotted markers and interpolated line show the spatial mean for each ten-day bin. The
 416 square, grey markers indicate the sample size (number of nodes) included in the distribution at each time
 417 step, with a separate Y-axis shown on the right of each pane.

418 We computed the ice equivalent snow melt (snow–ice equivalent; SIE) using Eq. 1:
 419

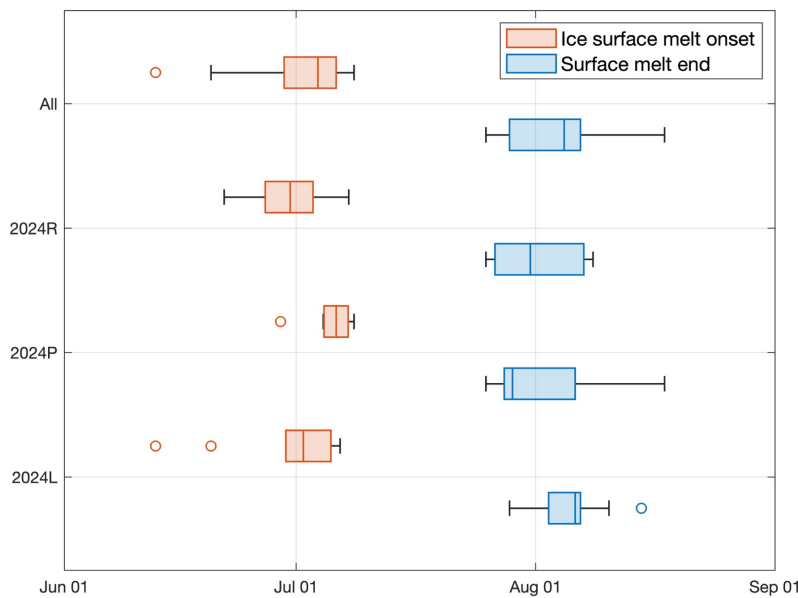
$$420 H_{\text{sie}} = \rho_s / \rho_i * H_{\text{snow}}, \quad (1)$$

421 where ρ_i is the density of sea ice (0.9 g cm^{-3} , Perovich et al., 2003), ρ_s is the density of snow (0.3 g cm^{-3} , Sturm et
 422 al., 2002), H_{snow} is the observed snow melt, and H_{sie} is the SIE melt. We combined H_{sie} with the observed ice
 423 surface melt to determine the total ice equivalent surface melt for each station. Average ice-equivalent melt was 0.33
 424 m at L, 0.31 m at P and 0.30 m at R, indicating very similar net surface melt across the region. Net ice-only surface
 425 melts were also quite similar with 0.23 m at L, 0.20 m at P and 0.23 m at R. The network with the deepest initial
 426 snow depth (P) also had the smallest ice melt, presumably because deeper snow increased albedo and physically

427 protected the ice, delaying surface melt onset (Fig. 9). Compared to variability between regions or years within the
428 Arctic (e.g., Perovich (2014) or Planck (2022)), however, these variations in mean behavior are quite small.

429 A key note here is that variability in surface melt (both ice surface melt and combined equivalent melt) was
430 relatively low *between* networks, the largest variability being a 13% difference in ice surface melt between R and P
431 (R higher), and a 9% difference in combined equivalent melt between L and R (L higher). However, melt variability
432 *within* networks was higher, at 31–46% for ice surface melt, and 15–38% for combined equivalent melt. This
433 suggests that networks of this size (on the order of ten nodes) may be adequate for accurately capturing the local
434 variability of surface melt. [We note that the surface melt variability seen here was lower than on SHEBA and](#)
435 [MOSAiC, where the maximum differences in observed surface ice melt were 55% and 71% \(Perovich, 2002;](#)
436 [Raphael, 2024\). We recommend a more thorough evaluation of the number of stations required to capture surface](#)
437 [melt variability.](#)

438 Snow accumulation began soon after the conclusion of surface melt, in early to mid August. Network L
439 saw 0.08 m snow accumulation by 16 October, then a decrease to 0.04 m snow depth by 26 October, when the
440 network ceased reporting. The air temperature record suggests that the decrease was caused by wind removal rather
441 than surface melt. Network R saw 0.14 m of new snow by 15 November, when it also ceased returning data. As of 3
442 January, 2025, network P has seen a mean snow accumulation of 0.39 m and a range of 0.12–0.80 m.



443

444 **Figure 9: Box-and-whisker plot showing the distribution of ice surface melt onset and surface melt end**
445 **dates.** Ice surface melt onset is shown in orange, and surface melt end is shown in blue for the nodes within
446 each network. Network 2024O is excluded since the network stopped reporting before surface melt onset.
447 “All” shows the combined distribution of all active nodes in 2024R, 2024P, and 2024L.

448
449 Despite relatively small geographical separation, snow accumulation varied significantly between
450 networks. We compare the snow accumulation at networks L, P, and R during the period from freezeup around early
451 August, through 26 October, when network L failed. The networks were deployed within 113 km of each other, and
452 by 26 October, networks L and P were still within 98 km of each other. Meanwhile, network R drifted to 306 km
453 from network L, and 398 km from network P. During this period, 0.04 m of snow accumulated at network L, 0.25 m
454 of snow accumulated at network P, and 0.14 m of snow accumulated at network R. This indicates a roughly 84%
455 difference in snow accumulation between networks L and P in that period, despite their relative proximity.

456 Further, the variability of snow accumulation within each network is evident in the widening box-and-
457 whisker distributions in Fig. 8. This variability increases as accumulation continues through the winter at network R
458 and, in particular, at network P. The attrition of nodes at network P during this period prompted us to consider
459 whether the increase in the interquartile range (IQR) is an artifact of the declining sampling size or a real signal.
460 Because the increase in IQR occurs primarily during a period when the sample size is constant ($n = 4$), we suggest
461 that the increase in the IQR is a real signal that is amplified by the small sample size.

462 Finally, the range of snow depth on 26 October was approximately equal to the range at time of installation
463 for network L, slightly higher at network R, and substantially higher at network P. This is potentially the result of
464 both interannual as well as spatial variability (due to ice advection).

465 As many studies have confirmed, snow depth on sea ice is highly variable; this case study suggests that
466 SnoTATOS can observe that variability, though the number of nodes needed to fully constrain it is unclear. In order
467 to facilitate efficient use of resources and enable accurate, error-constrained data collection, we recommend further
468 research into the number and arrangement of sampling points needed to measure the spatial and temporal variability
469 of the snow cover on Arctic sea ice. Such a study should investigate the errors produced when using various sample
470 sizes and patterns to estimate snow depth mean and variance at the floe scale, and, ultimately, identify the minimum
471 number of stations typically needed to constrain these statistics. Sturm (2009) conducted a limited study by
472 resampling snow depth transect data with consecutively decreasing sample sizes, however, this study was limited to
473 three, one-dimensional transects, all collected in the same location on the same date. A similar, more extensive study
474 should be undertaken by resampling data collected across multiple locations, instances, and ice types. We also
475 suggest testing various spatial arrangements of the sample points (random, gridded, etc.).

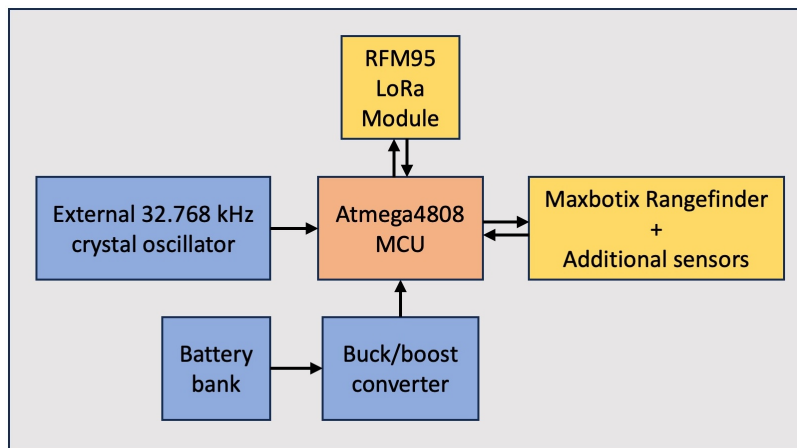
476 4 Conclusions

477 This work documents the development, testing, and a case study deployment of SnoTATOS, a new autonomous
478 system for collecting distributed, in situ snow depth measurements on sea ice. Responding to community calls for
479 the widespread snow depth measurements that are needed to understand the changing Arctic sea ice system, and
480 recognizing the lack of suitable, affordable tools, we set out to create a low-cost, easy-to-use system to fill the gap.
481 The resulting radio-networked snow depth measurement stations are only 5% of the cost and 7% of the weight of

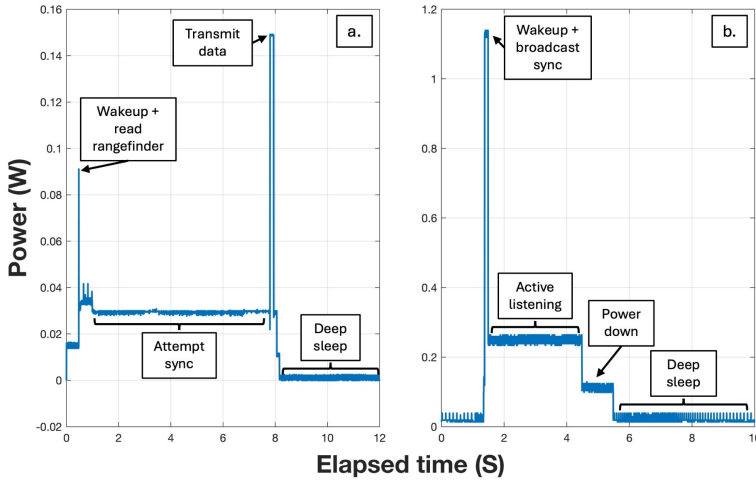
482 existing systems, with identical measurement functionality. A case study deployment of four SnoTATOS networks
483 in the Lincoln Sea in April 2024 1) validates the functionality of SnoTATOS, including the system's ease of
484 transport, rapid installation, and collection of high-quality, in situ snow depth and surface melt measurements, 2)
485 demonstrates the substantial spatial and temporal variability in snow accumulation and ice surface melt at the floe
486 scale, and 3) suggests that even relatively small SnoTATOS networks (on the order of 10 nodes) are capable of
487 capturing that variability. Based on the last finding, we recommend focused studies to determine the number and
488 placement of autonomous sampling stations needed to accurately capture snow accumulation, depth, and surface
489 melt variability.

490 Of the forty nodes installed in April 2024, four were still reporting by the beginning of January 2025. The
491 character of the failures suggests most (26) failed by physical damage. High attrition rates resulting from ice
492 dynamics and wildlife are a reality for autonomous instruments installed on Arctic sea ice. This, in addition to a
493 need for more comprehensive observations of Arctic variability, is a strong motivation to transition towards the use
494 of large, redundant networks of lightweight, inexpensive sensing stations, an approach also recommended by Lee et
495 al. (2022) and Webster et al. (2022). In its current permutation, SnoTATOS can accommodate additional sensors
496 such as barometric pressure or temperature sensors. We plan to build on this technology to create a modular “polar
497 Internet of Things” sensing system capable of hosting plug-and-play sensors, making radio-networked distributed
498 sensing more accessible for the polar regions. We anticipate that SnoTATOS will also prove useful for monitoring
499 snow accumulation and ice surface melt in alpine, glacier, and tundra environments.

500 **Appendix A: sensing unit components and power test**



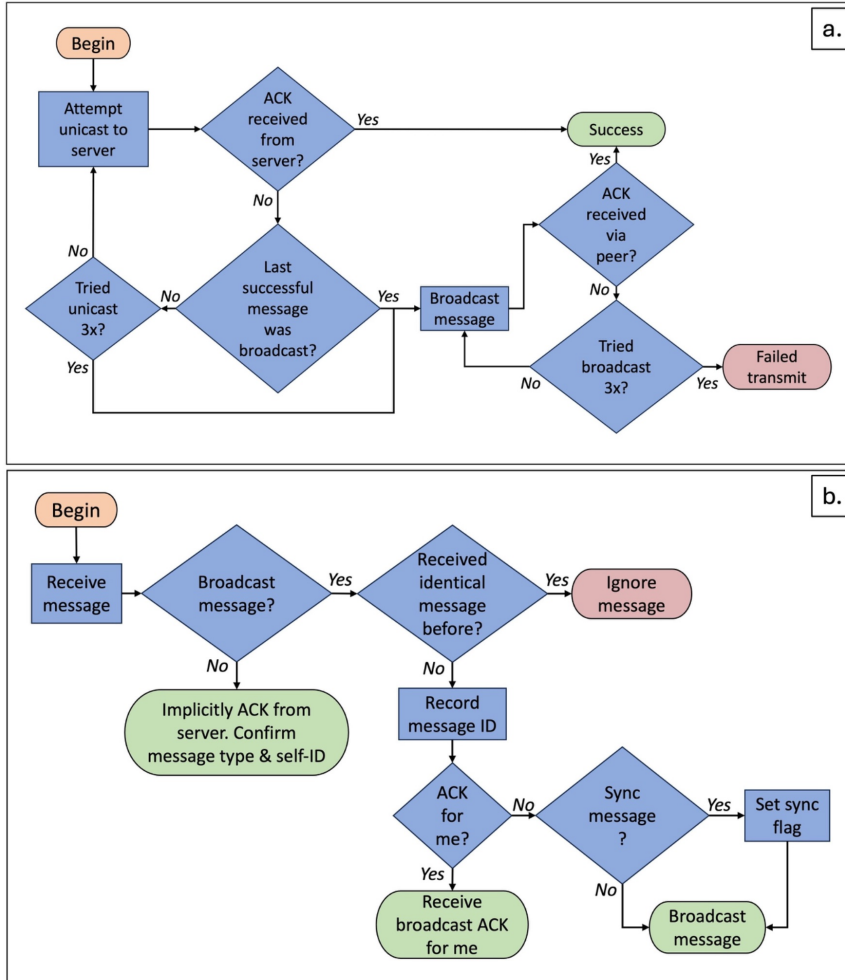
501
502 **Figure A1: Schematic block diagram of SnoTATOS sensing unit electronics.** The figure shows the
503 major electronics components of the SnoTATOS sensing unit. Blue blocks indicate external power and
504 clock components for the MCU, which is shown in orange. Yellow blocks indicate I/O modules that the
505 MCU interacts with for collecting and transmitting data.



506
 507 **Figure A2: Time-resolved power demand for the node and server during pre-deployment bench**
 508 **testing.** Panel (a.) shows the power demand during the various stages of the duty cycle for a node with $V_s =$
 509 2.4 V . Panel (b.) shows the power demand during the various stages of the duty cycle for the server with
 510 $V_s = 18 \text{ V}$.

511 **Appendix B: mesh network implementation**

512 The node-side logical flow for mesh network packet handling is shown in Fig. B1. During a data transmission
 513 attempt, a node will first attempt to unicast the message directly to the server. If an acknowledgment (ACK) is
 514 received, then the message has been transmitted successfully and the attempt ends. If an ACK is not received within
 515 a timeout period, the node then reattempts transmission, either repeating a unicast if the last ACK'd message was
 516 *not* a broadcast, or progressing directly to broadcast attempts if the node knows that the last message it successfully
 517 transmitted to the server was a broadcast message. If an ACK is not received within the allotted number of
 518 reattempts, or the timeout period expires, then the transmission attempt has failed. The attempt ends, and it is
 519 counted towards the number of allowable failed transmissions before the node is prompted to resync with the server.



520

521 **Figure B1: Logical flow diagram for node-side mesh network packet handling.** Panel (a.) shows the
 522 logical flow for handling a mesh network message transmission attempt. Panel (b.) shows the logical flow
 523 for handling a received mesh network message.

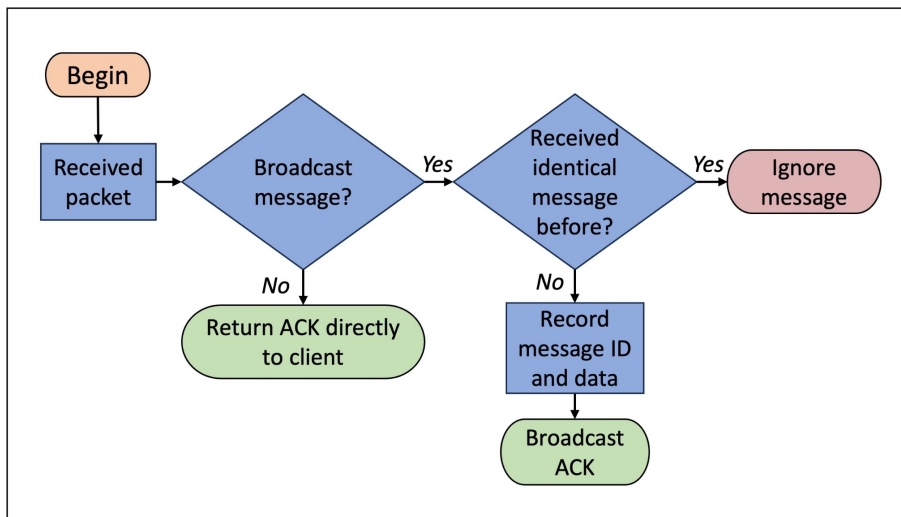
524

525 In the mesh network model, whenever a node receives a message, it first checks whether it is a broadcast
 526 message. If it is not a broadcast message, it is implicitly a unicast ACK message from the server. The node confirms
 527 that it is an ACK message and that it is addressed to itself, and if so, records the acknowledgement. If it is a
 528 broadcast message (either from the server or via a peer), and it is not a message that it has already received, the node
 529 will first note the message ID, then process the message contents. If it is addressed to itself, it is implicitly a

530 broadcast ACK message originating from the server (likely received via a peer). If the node confirms that it is an
 531 ACK message with its own address, it records the acknowledgement. If it is not addressed to itself, it could be a data
 532 message originating from a peer and addressed to the server; an ACK message originating from the server and
 533 addressed to a peer, or a sync message originating from the server and addressed to the entire network. In the first
 534 two cases, the node rebroadcasts the message without further processing. In the latter (sync) case, the node first sets
 535 its synchronization flag, then rebroadcasts the message to the network.

536 In a mesh topology network, the server follows the logical flow shown in Fig. B2. First, the server checks
 537 to see if the received message is a broadcast or unicast message. If it is unicast, the server returns a unicast ACK. If
 538 it is a broadcast message, and if it is not a repeat message, the server broadcasts an ACK message addressed to the
 539 originating node.

540



541
 542 **Figure B2: Logical flow diagram for server-side mesh network packet handling.** The logical flow for
 543 receiving a mesh network message and returning an acknowledgement is shown.

544 Data accessibility

545 SnoTATOS data from the Lincoln Sea case study have been [archived](#) at the Arctic Data Center and [are available at](#):
 546 doi:10.18739/A2FJ29F6X.

547 Author Contributions

548 IAR, DKP, and CMP conceived the study. IAR designed and built the system under study with supervision and
 549 feedback from DKP, CMP, and RLH. CMP deployed the sensors. IAR drafted the manuscript. All authors
 550 contributed to editing and review. All authors approved the manuscript for submission.

Deleted: submitted for archive
Deleted: will be
Deleted: upon archive publication
Deleted: A2RX93G1Q

555 **Competing Interests**

556 The authors declare that they have no conflict of interest.

557 **Acknowledgements**

558 We thank Nathan Kurtz, Patrick Taylor, and the NASA ARCSIX team for collaboration and funding support. We
559 thank Patricia Nelsen and Leroy Hessner on the ARCSIX deployment team, pilots Troy McKerrel and Griffin Kelly,
560 and the Kenn Borek air team. We thank the Governments of Canada and Greenland and the staff at Eureka,
561 Nord/Villum, and CFS Alert Stations for their hospitality and substantial assistance in making the ARCSIX
562 deployment possible. We thank David Clemens-Sewall for his contributions to an early version of SnoTATOS, and
563 for subsequent conversations and suggestions that greatly improved the system. We thank Marcel Nicolaus for
564 similar conversations and critical feedback, and for his help deploying an early version of the system on the
565 ARCWATCH expedition. We thank Mario Hoppmann, whose parallel work on distributed snow and ice sensing
566 systems helped inform SnoTATOS development, for his feedback on early versions of the system, and for his help
567 in the field on the ARCWATCH expedition. We thank Jan Rohde for thought-provoking discussions about sensor
568 development and engineering for Arctic science, and for his assistance in the lab and in the field on the
569 ARCWATCH expedition. We thank Larson Kaidel, Harvard Brown, Ben Elavgak, and UIC Science for their
570 support in deploying a prototype version of SnoTATOS in Utqiagvik in November 2022.

571 **Financial Support**

572 IAR received support from the National Defense Science and Engineering Graduate Fellowship. IAR and DKP
573 received financial support from NSF OPP-2034919 and NOAA projects 1305M322PNRMT0632 and
574 NA24OARX431G0018. CMP received financial support from NSF OPP-2034919, NASA-ARCSIX under IAA-
575 80GSFC23TA046, and the ERDC-CRREL ISOPS program.

576 **References**

577 HRXL-MaxSonar-WR Datasheet: <https://maxbotix.com/pages/hrxl-maxsonar-wr-datasheet>, last access: 20 May
578 2024.

579

580 RadioLib - Arduino Reference: <https://www.arduino.cc/reference/en/libraries/radiolib/>, last access: 20 May 2024.

581

582 Augustin, A., Yi, J., Clausen, T., and Townsley, W. M.: A Study of LoRa: Long Range & Low Power Networks for
583 the Internet of Things, Sensors, 16, 1466, <https://doi.org/10.3390/s16091466>, 2016.

584

585 Backus, G.: Arctic 2030: What are the consequences of climate change?: The US response, Bull. At. Sci., 68, 9–16,
586 <https://doi.org/10.1177/0096340212451568>, 2012.

587

588 Barnhart, K. R., Overeem, I., and Anderson, R. S.: The effect of changing sea ice on the physical vulnerability of
589 Arctic coasts, The Cryosphere, 8, 1777–1799, <https://doi.org/10.5194/tc-8-1777-2014>, 2014.

590

591 Bystrowska, M.: The Impact of Sea Ice on Cruise Tourism on Svalbard, Arctic, 72, 151–165, 2019.

592

593 Carman, J. C.: Economic and Strategic Implications of Ice-Free Arctic Seas, 2002.

594

595 Clemens-Sewall, D., Polashenski, C., Raphael, I. A., Parno, M., Perovich, D., Itkin, P., Jaggi, M., Jutila, A.,
596 Macfarlane, A. R., Matero, I. S. O., Oggier, M., Visser, R. J. W., and Wagner, D. N.:
597 High-resolution repeat topography of drifting ice floes in the Arctic Ocean from terrestrial laser scanning, Sci. Data,
598 11, 70, <https://doi.org/10.1038/s41597-023-02882-w>, 2024a.

599

600 Clemens-Sewall, D., Polashenski, C., Perovich, D., and Webster, M. A.: The importance of sub-meter-scale snow

601 roughness on conductive heat flux of Arctic sea ice, *J. Glaciol.*, <https://doi.org/10.1017/jog.2023.105>, 2024b.

602

603 Colony, R., Radionov, V., and Tanis, F. J.: Measurements of precipitation and snow pack at Russian North Pole

604 drifting stations, *Polar Rec.*, 34, 3–14, <https://doi.org/10.1017/S0032247400014923>, 1998.

605

606 Duncan K., Farrell S.L., Connor L.N., Richter-Menge J., Hutchings J.K., Dominguez R.: High-resolution airborne

607 observations of sea-ice pressure ridge sail height, *Annals of Glaciology*, 59,137-147, doi:10.1017/aog.2018.2, 2018.

608

609 Eicken, H. and Mahoney, A. R.: Chapter 13 - Sea Ice: Hazards, Risks, and Implications for Disasters, in: *Coastal*

610 and *Marine Hazards, Risks, and Disasters*, edited by: Shroder, J. F., Ellis, J. T., and Sherman, D. J., Elsevier,

611 Boston, 381–401, <https://doi.org/10.1016/B978-0-12-396483-0.00013-3>, 2015.

612

613 Fetcenko, M. A., Ovshinsky, S. R., Reichman, B., Young, K., Fierro, C., Koch, J., Zallen, A., Mays, W., and Ouchi,

614 T.: Recent advances in NiMH battery technology, *J. Power Sources*, 165, 544–551,

615 <https://doi.org/10.1016/j.jpowsour.2006.10.036>, 2007.

616

617 Gerland, S., Barber, D., Meier, W., Mundy, C. J., Holland, M., Kern, S., Li, Z., Michel, C., Perovich, D. K., and

618 Tamura, T.: Essential gaps and uncertainties in the understanding of the roles and functions of Arctic sea ice,

619 *Environ. Res. Lett.*, 14, 043002, <https://doi.org/10.1088/1748-9326/ab09b3>, 2019.

620

621 Granskog, M. A., Fer, I., Rinke, A., and Steen, H.: Atmosphere-Ice-Ocean-Ecosystem Processes in a Thinner Arctic

622 Sea Ice Regime: The Norwegian Young Sea ICE (N-ICE2015) Expedition, *J. Geophys. Res. Oceans*, 123, 1586–

623 1594, <https://doi.org/10.1002/2017JC013328>, 2018.

624

625 Holland, M. M., Clemens-Sewall, D., Landrum, L., Light, B., Perovich, D., Polashenski, C., Smith, M., and

626 Webster, M.: The influence of snow on sea ice as assessed from simulations of CESM2, *The Cryosphere*, 15, 4981–

627 4998, 2021.

628

629 Iacozza, J. and Barber, D. G.: An examination of the distribution of snow on sea-ice, *Atmosphere - Ocean*, 37, 21–

630 51, <https://doi.org/10.1080/07055900.1999.9649620>, 1999.

631

632 Itkin, P., Spreen, G., Cheng, B., Doble, M., Girard-Ardhuin, F., Haapala, J., Hughes, N., Kaleschke, L., Nicolaus,

633 M., and Wilkinson, J.: Thin ice and storms: Sea ice deformation from buoy arrays deployed during N-ICE 2015, *J.*

634 *Geophys. Res. Oceans*, 122, 4661–4674, 2017.

635

636 Itkin, P., Hendricks, S., Webster, M., Albedyll, L. von, Arndt, S., Divine, D., Jaggi, M., Oggier, M., Raphael, I.,

637 Ricker, R., and others: Sea ice and snow characteristics from year-long transects at the MOSAiC Central

638 Observatory, *Elem. Sci. Anthr.*, 11, 2023.

639

640 Itkin, P. and Liston, G. E.: Combining observational data and numerical models to obtain a seamless high temporal

641 resolution seasonal cycle of snow and ice mass balance at the MOSAiC Central Observatory, EGUspHERE [preprint],

642 <https://doi.org/10.5194/egusphere-2024-3402>, 2024.

643

644 Jahn, A., Holland, M. M., and Kay, J. E.: Projections of an ice-free Arctic Ocean, *Nat. Rev. Earth Environ.*, 5, 164–

645 176, <https://doi.org/10.1038/s43017-023-00515-9>, 2024.

646

647 Kwok, R.: Arctic sea ice thickness, volume, and multiyear ice coverage: losses and coupled variability (1958–2018),

648 *Environ. Res. Lett.*, 13, 105005, 2018.

649

650 Laidre, K. L., Stern, H., Kovacs, K. M., Lowry, L., Moore, S. E., Regehr, E. V., Ferguson, S. H., Wiig, Ø., Boveng,

651 P., Angliss, R. P., Born, E. W., Litovka, D., Quakenbush, L., Lydersen, C., Vongraven, D., and Ugarte, F.: Arctic

652 marine mammal population status, sea ice habitat loss, and conservation recommendations for the 21st century,

653 *Conserv. Biol.*, 29, 724–737, <https://doi.org/10.1111/cobi.12474>, 2015.

654

655 Lee, C., DeGrandpre, M., Guthrie, J., Hill, V., Kwok, R., Morison, J., Cox, C., Singh, H., Stanton, T., and

656 Wilkinson, J.: Emerging Technologies and Approaches for In Situ, Autonomous Observing in the Arctic,

657 Oceanography, <https://doi.org/10.5670/oceanog.2022.127>, 2022.

658

659 Liao, Z., Cheng, B., Zhao, J., Vihma, T., Jackson, K., Yang, Q., Yang, Y., Zhang, L., Li, Z., Qiu, Y., and Cheng, X.:
660 Snow depth and ice thickness derived from SIMBA ice mass balance buoy data using an automated algorithm, *Int. J.*
661 *Digit. Earth*, 12, 962–979, <https://doi.org/10.1080/17538947.2018.1545877>, 2019.

662

663 McNamee, E.: NASA Mission Flies Over Arctic to Study Sea Ice Melt Causes, NASA, 31st May, 2024.

664

665 Meier, W. N. and Markus, T.: Remote sensing of sea ice, in: *Remote Sensing of the Cryosphere*, John Wiley &
666 Sons, Ltd, 248–272, <https://doi.org/10.1002/9781118368909.ch11>, 2015.

667

668 Meier, W. N., Petty, A., Hendricks, S., Kaleschke, L., Divine, D., Farrell, S., Gerland, S., Perovich, D., Ricker, R.,
669 Tian-Kunze, X., and Webster, M.: *NOAA Arctic Report Card 2023: Sea Ice*, NOAA, 2023.

670

671 Merkouriadi, I., Gallet, J.-C., Graham, R. M., Liston, G. E., Polashenski, C., Rösel, A., and Gerland, S.: Winter
672 snow conditions on Arctic sea ice north of Svalbard during the Norwegian young sea ICE (N-ICE2015) expedition,
673 *J. Geophys. Res. Atmospheres*, 122, 10,837–10,854, <https://doi.org/10.1002/2017JD026753>, 2017.

674

675 *National Snow and Ice Data Center. (2004). Morphometric Characteristics of Ice and Snow in the Arctic Basin:
676 Aircraft Landing Observations from the Former Soviet Union, 1928-1989. (G02140, Version 1). Romanov, I. P.
677 (Comp.) [Data Set]. Boulder, Colorado USA. National Snow and Ice Data
678 Center. <https://doi.org/10.7265/N5B8562T>. Date Accessed 04-22-2025.*

679

680 Nicolaus, M., Hoppmann, M., Arndt, S., Hendricks, S., Katlein, C., Nicolaus, A., Rossmann, L., Schiller, M., and
681 Schwegmann, S.: Snow Depth and Air Temperature Seasonality on Sea Ice Derived From Snow Buoy
682 Measurements, *Front. Mar. Sci.*, 8, <https://doi.org/10.3389/fmars.2021.655446>, 2021.

683

684 Nicolaus, M., Perovich, D. K., Spreen, G., Granskog, M. A., Albedyll, L. von, Angelopoulos, M., Anhaus, P., Arndt,
685 S., Belter, H. J., Bessonov, V., and others: Overview of the MOSAiC expedition: Snow and sea ice, *Elem Sci Anth*,
686 10, 46, 2022.

687

688 Onarheim, I. H., Eldevik, T., Smedsrød, L. H., and Stroeve, J. C.: Seasonal and Regional Manifestation of Arctic
689 Sea Ice Loss, *J. Clim.*, 31, 4917–4932, <https://doi.org/10.1175/JCLI-D-17-0427.1>, 2018.

690

691 Patterson, D. A.: Reduced instruction set computers, *Commun. ACM*, 28, 8–21,
692 <https://doi.org/10.1145/2465.214917>, 1985.

693

694 Peng, G. and Meier, W. N.: Temporal and regional variability of Arctic sea-ice coverage from satellite data, *Ann.
695 Glaciol.*, 59, 191–200, 2018.

696

697 Perovich, D., Richter-Menge, J., Polashenski, C., Elder, B., Arbetter, T., and Brennick, O.: Sea ice mass balance
698 observations from the North Pole Environmental Observatory, *Geophys. Res. Lett.*, 41, 2019–2025, 2014.

699

700 Perovich, D., Raphael, I., Moore, R., Clemens-Sewall, D., Polashenski, C., and Planck, C.: Measurements of ice
701 mass balance and temperature from autonomous Seasonal Ice Mass Balance buoys in the Arctic Ocean, 2019–2020,
702 *Arct. Data Cent.*, 2022.

703

704 Perovich, D. K., Andreas, E. L., Curry, J. A., Eiken, H., Fairall, C. W., Grenfell, T. C., Guest, P. s., Intrieri, J.,
705 Kadko, D., Lindsay, R. W., McPhee, M. G., Morison, J., Moritz, R. E., Paulson, C. A., Pegau, W. S., Persson, P. o.
706 g., Pinkel, R., Richter-Menge, J. A., Stanton, T., Stern, H., Sturm, M., Tucker III, W. b., and Uttal, T.: Year on ice
707 gives climate insights, *Eos Trans. Am. Geophys. Union*, 80, 481–486, <https://doi.org/10.1029/EO080i041p00481-01>, 1999.

708

709 Perovich, D. K., Grenfell, T. C., Richter-Menge, J. A., Light, B., III, W. B. T., and Eicken, H.: Thin and thinner: Sea
710 ice mass balance measurements during SHEBA, *J. Geophys. Res. Oceans*, 108, 2003.

711

712

713 Planck, C. J.: Observing and Analyzing Arctic Sea Ice Mass Balance Using Autonomous Systems, Ph.D.,
714 Dartmouth College, United States -- New Hampshire, 151 pp., 2021.
715

716 Planck, C. J., Whitlock, J., Polashenski, C., and Perovich, D.: The evolution of the seasonal ice mass balance buoy,
717 Cold Reg. Sci. Technol., 165, 2019.
718

719 Polashenski, C., Perovich, D., and Courville, Z.: The mechanisms of sea ice melt pond formation and evolution, J.
720 Geophys. Res. Oceans, 117, 2012.
721

722 Post, E., Bhatt, U. S., Bitz, C. M., Brodie, J. F., Fulton, T. L., Hebblewhite, M., Kerby, J., Kutz, S. J., Stirling, I.,
723 and Walker, D. A.: Ecological Consequences of Sea-Ice Decline, Science, 341, 519–524,
724 <https://doi.org/10.1126/science.1235225>, 2013.
725

726 Rabe, B., Cox, C. J., Fang, Y.-C., Goessling, H., Granskog, M. A., Hoppmann, M., Hutchings, J. K., Krumpen, T.,
727 Kuznetsov, I., Lei, R., Li, T., Maslowski, W., Nicolaus, M., Perovich, D., Persson, O., Regnery, J., Rigor, I., Shupe,
728 M. D., Sokolov, V., Spreeen, G., Stanton, T., Watkins, D. M., Blockley, E., Buenger, H. J., Cole, S., Fong, A.,
729 Haapala, J., Heuzé, C., Hoppe, C. J. M., Janout, M., Jutila, A., Kattlein, C., Krishfield, R., Lin, L., Ludwig, V.,
730 Morgenstern, A., O'Brien, J., Zurita, A. Q., Rackow, T., Riemann-Campe, K., Rohde, J., Shaw, W., Smolyanitsky,
731 V., Solomon, A., Sperling, A., Tao, R., Toole, J., Tsamados, M., Zhu, J., and Zuo, G.: The MOSAiC Distributed
732 Network: Observing the coupled Arctic system with multidisciplinary, coordinated platforms, Elem. Sci. Anthr., 12,
733 00103, <https://doi.org/10.1525/elementa.2023.00103>, 2024.
734

735 ~~Raphael, I.A., Perovich, D.K., Polashenski, C.M., Clemens-Sewall, D., Itkin, P., Lei, R., Nicolaus, M., Regnery, J.,
736 Smith, M.M., Webster, M., Jaggi, M.: Sea ice mass balance during the MOSAiC drift experiment: Results from
737 manual ice and snow thickness gauges. *Elementa: Science of the Anthropocene* 12(1).~~
738 DOI: <https://doi.org/10.1525/elementa.2023.00040>, 2024.

739

740 ~~Raphael, I., Perovich, D., and Polashenski, P.: Snow Thickness and Temperature Observation System (SnoTATOS)
741 snow depth and surface melt observations from the 2024 Arctic Radiation Cloud Aerosol Surface Interaction
742 Experiment (ARCSIX) campaign, Lincoln Sea. Arctic Data Center. doi:10.18739/A2FJ29F6X, 2025.~~
743

744 Rösel, A., Itkin, P., King, J., Divine, D., Wang, C., Granskog, M. A., Krumpen, T., and Gerland, S.: Thin sea ice,
745 thick snow, and widespread negative freeboard observed during N-ICE2015 north of Svalbard, J. Geophys. Res.
746 Oceans, 123, 1156–1176, 2018.
747

748 Sturm, M., Holmgren, J., and Perovich, D. K.: Winter snow cover on the sea ice of the Arctic Ocean at the Surface
749 Heat Budget of the Arctic Ocean (SHEBA): Temporal evolution and spatial variability, J. Geophys. Res. Oceans,
750 107, SHE 23-1-SHE 23-17, <https://doi.org/10.1029/2000JC000400>, 2002.
751

752 ~~Sturm, M.: Field techniques for snow observations on sea ice, in *Field techniques for sea ice research*, 25–47, 2009.~~
753

754 Webster, M., Gerland, S., Holland, M., Hunke, E., Kwok, R., Lecomte, O., Massom, R., Perovich, D., and Sturm,
755 M.: Snow in the changing sea-ice systems, Nat. Clim. Change, 8, 946–953, [https://doi.org/10.1038/s41558-018-0286-7](https://doi.org/10.1038/s41558-018-
756 0286-7), 2018.
757

758 Webster, M. A., Rigor, I., and Wright, N. C.: Observing Arctic Sea Ice, Oceanography, 35, 28–37,
759 <https://doi.org/10.5670/oceanog.2022.115>, 2022.
760

761 Zahn, T., O'Shea, G., and Rowstron, A.: An empirical study of flooding in mesh networks, ACM SIGMETRICS
762 Perform. Eval. Rev., 37, 57–58, <https://doi.org/10.1145/1639562.1639584>, 2009.
763

764 Zampieri, L., Clemens-Sewall, D., Sledd, A., Hutter, N., and Holland, M.: Modeling the Winter Heat Conduction
765 Through the Sea Ice System During MOSAiC, Geophys. Res. Lett., 51, e2023GL106760,
766 <https://doi.org/10.1029/2023GL106760>, 2024.
767

768 Zimmermann, H.: OSI Reference Model - The ISO Model of Architecture for Open Systems Interconnection, IEEE

Deleted: 

... [1]

Formatted: Font: Not Italic, Complex Script Font: Not Italic

